HiSST: 2nd International Conference on
High-Speed Vehicle Science & Technology
11–15 September 2022, Bruges, Belgium

Analysis of Weather Balloon Data to Evaluate the Aerodynamic Influence on the Launch Phase of SHEFEX II

Marius Franz[1] *Philipp Donn*[2]

Abstract

In this work, an advanced atmospheric model (IATM) for the flight of SHEFEX II is created and its effect on the aerodynamic loads of the first stage fins of SHEFEX II is investigated. The atmospheric model bases on weather balloon data collected at the starting day of the flight experiment. The wind data are decomposed using empirical mode decomposition (EMD) and reduced by their intrinsic mode functions (IMF) to get wind data without balloon oscillation. Compared to a linear interpolated atmosphere (LATM) the numerical results show no significant influence on the forced motion body loads but there is a high impact of wind on the fins of SHEFEX II as unsteady simulations show an increase up to twice the amount of dynamic loading, while viscous effects can be neglected.

Keywords: *SHEFEX II, CFD, CFM, Coupling, Trajectory, Atmosphere, Wind*

Nomenclature

Latin
ATM – atmospheric model
C – dimensionless coefficient
EMD – empirical mode decomposition
F – force
GCI – grid convergence index
h – altitude
IMF – intrinsic mode functions
M – moment
Ma – mach number
p – pressure
PSD – power spectral density
r – roll rate
R – refinement factor
t – time
TPS – thermal protection system
U – velocity

Greek
α – angle of attack
δ – fin deflection angle
Δ – absolute difference
ϵ – relative error
Superscripts
W – wind
Subscripts
C – coarse
f – fin
F – fine
N – normal
STOP – abort criteria
w – wind
x – x-direction (tail to nose)
y – y-direction (starboard)
z – y-direction (downwards)

1. Introduction

During the development and design phase of spacecrafts adequate aerodynamic and structural simulations are crucial for stable and high performing sounding rockets and re-entry vehicles. Higher payloads often can only be achieved by decreasing the structural mass which, on the other hand, increases the risk of a structural failure. As failure is not an option for such costly experiments the modelling effort and level of detail has been increased over the years.

Possible savings in thermal protection system (TPS) costs directly influenced the main idea of the Sharp Edge Flight Experiment (SHEFEX). As a result, a sharp edged geometry for the TPS and the geometry

[1] *Institute of Aerodynamics and Flow Technology, DLR, German Aerospace Center, Marius.Franze@dlr.com*
[2] *TU Carolo-Wilhelmina zu Braunschweig, Brunswick, Germany*

Copyright © 2022 by the author(s)

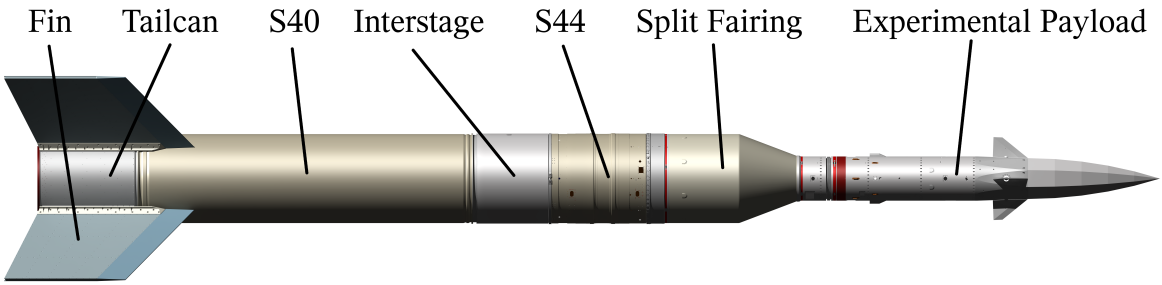

Fig 1. Schematic representation of the SHEFEX II vehicle.

of the vehicle itself was developed as shown in Eggers et al. [2]. The post flight analysis of SHEFEX I, launched in 2007, showed significant fin deformations during the experimental ascend phase. Those antisymmetric deformations resulted in an added roll rate influencing the flown flight path significantly, as shown by Calvo and Eggers [1]. The preceding post flight analysis of SHEFEX II made by Franze [3, 4] showed a similar behaviour although the fins got bigger and reinforced compared to SHEFEX I. Nevertheless the fins deformed as well by about $\Delta\delta_f = 0.15°$, which will result in different free flight simulation data.

To get more into detail of the aerodynamic loads on the structure during the ascent phase, this work will extract wind data from the measured weather balloon data and afterwards filter it via EMD to reduce the amount of measurement errors due to balloon oscillation. To compare the differences in the calculated atmosphere, dynamic forced oscillation URANS simulations are performed, with and without viscous effects.

The first section presents in short the SHEFEX II vehicle and the measurement setup for the weather balloons. The second part briefly explains the used numeric codes and methods, including a mesh convergence study. The third section presents the analytic and numerical result. Finally, a summary of the collected results and an outlook for future proceeding is given.

2. Description of the Vehicle, Flight Data and Weather Balloon Setup

2.1. Experimental Vehicle

SHEFEX II was successfully launched at 19:18 UTC on 22nd June 2012 from the Andøya Rocket Range (ARR) near Andenes in Norway. The apogee was reached at an altitude of 178 km after 5 minutes and it landed 8 minutes later into the north polar sea where it was not recovered due to high waves at the landing side.

The two staged rocket, shown in Figure 1, consists of a Brazilian S40 motor as first and a S44 motor as second stage, connected by an interstage adapter. The nominal set fin angle is $\delta_{nom} = 0.6°$ for roll stabilization during the ascend phase. The final roll rate was about $r = 1.6$ Hz. SHEFEX II was 12.7 m long and had a starting weight of 7058 kg. In preliminary flight performance studies the targeted Mach number during the experimental phase is between $9.5 < Ma < 11$ at an altitude of $100km > h > 20km$ [13]. The post processed flight trajectory is shown in an earlier work [3].

2.2. Weather Balloon Setup

On the flight day of SHEFEX II, seven weather balloons were launched from four different stations. From Andøya, Bjørnøya and Jan Mayen two balloons were launched each and a seventh balloon from the island of Spitsbergen. All weather balloon starting points are located along the estimated flight path of SHEFEX II so that a sufficient coverage of the atmospheric parameters is guaranteed. Figure 2 shows the chosen starting points. SHEFEX II flew along the yellow trajectory in direction north-north-west and passed the stations Bjørnøya and Jan Mayen during its reentry phase. The flown ground distance amounts to ca. 800 km [12]. Table 1 shows the introduced naming of each balloon, their maximum altitude of useful data as well as the used sampling rate. Each balloon recorded information about the

Copyright © 2022 by the author(s)

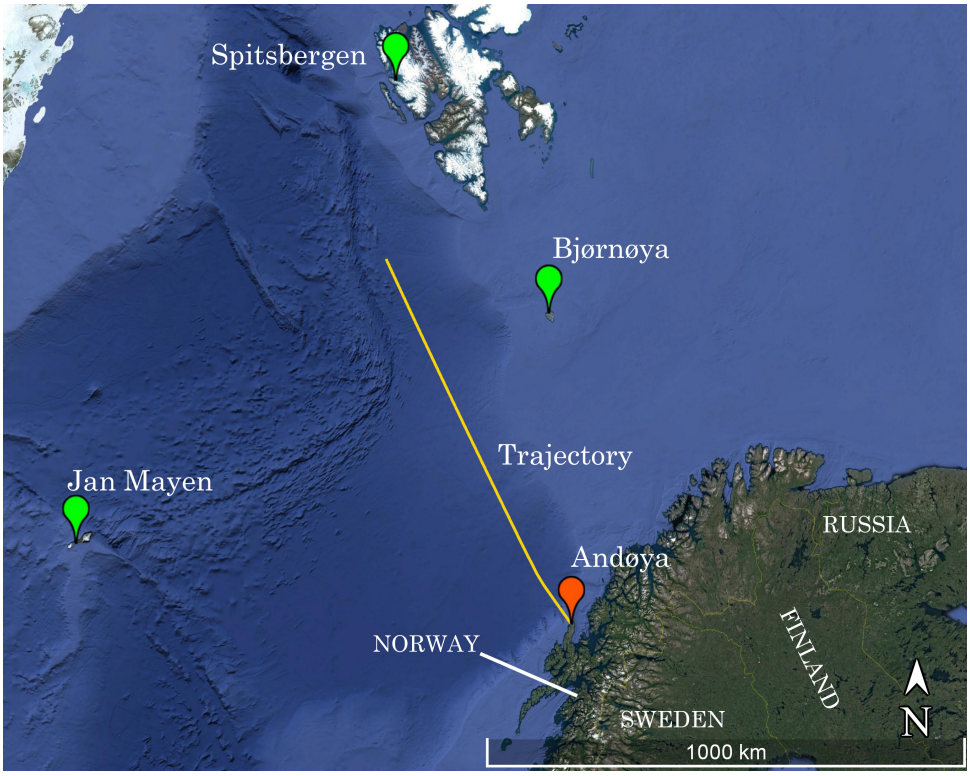

Fig 2. Location of the weather balloon stations along the estimated trajectory.

outer pressure and temperature, the relative humidity as well as the horizontal wind components. Their starting times differ slightly as the Spitsbergen balloon was launched about noon and all other balloons presumably in the afternoon of the flight day.

Table 1. Maximum altitude and sampling rate of the weather balloons.

	Andøya		**Bjørnøya**		**Jan Mayen**		**Spitsbergen**
	AND1	**AND2**	**BJO1**	**BJO2**	**JAN1**	**JAN2**	**SPI**
Altitude [m]	27 183	14 168	35 301	38 417	31 255	38 983	34 238
Sampling rate [Hz]	1	1	0.5	0.5	0.5	0.5	0.2

3. Numerical Methods

3.1. Unsteady Analysis of Trajectory using DLR TAU Code

This paper follows a two step approach in evaluating the influence of the different atmospheric models. Due to the fact that SHEFEX II spends most of its launch phase in a supersonic flow regime one can conclude that the viscous components of the forces will be negligible compared to the pressure induced components for most of the time. Hence, in a first step only inviscid Euler equations are solved to compensate for the high amount of analysed flight points. In a second step, Navier-Stokes simulations are performed in order to verify the obtained data and eradicate remaining questions from the inviscid calculations. However, all simulations feature the same general approach.

The unsteady Euler/Navier-Stokes equations including rigid body motion are solved using the DLR TAU code which is validated for subsonic, transonic and hypersonic flows [8, 6]. The completely parallelized code uses domain decompositioning via Message Passing Interface (MPI).

Copyright © 2022 by the author(s)

When solving the inviscid Euler equations, at first a second order central scheme with backward euler relaxation is used for the subsonic sections of the trajectory, but showed a very poor convergence behavior for Ma $>$ 0.5, which is referable to the big wake region of the vehicle where high shear layer fluctuations dominate the flow field. For this reasons a second order AUSMDV [11] upwind scheme with backward euler relaxation solver is used for the whole trajectory, meaning for both subsonic and supersonic regions the upwind scheme can be applied. However, the resulting forces differ just slightly between the central and upwind scheme at Ma $<$ 0.5 where both schemes perform well. The viscous uRANS (unsteady RANS) calculations where performed using a central scheme.

Computing 1000 iterations per unsteady dual time step of $\Delta t = 0.02\,s$ for the first 15 s to 22 s and 500 iterations afterwards until 55 s flight time the density residual reaches sufficiently low values to get a solution with converged aerodynamic coefficients. However, the latter is not strictly true for the transonic region as the aerodynamic coefficients showed a rather oscillating behaviour which could not be improved by increasing the number of iterations.

For the viscous URANS simulations the negative implementation of Spalart-Almaras model is used, as SHEFEX II is a rather simple geometry due to the sharp flow separating edges this simpler model is chosen over a more sophisticated one like Menter SST. Although the Mesh convergence study is performed with Menter SST as well, showing only a small difference between the models at Ma $=$ 0.4.

The following computations are produced by forcing the flight mechanic data by means of its position, orientation, flight velocity and roll rates, collected by the Hybrid Navigation System (HNS), presented by Steffes [9], onto an unsteady DLR TAU computation, changing the flight condition every time step $\Delta t = 0.02\,s$, to match the flown flight path, similar to a forced oscillation method. For this use case an external motion function was applied, implemented by Heinrich et al. [5]. This function allows to set the inflow condition to Ma $=$ 0 and move the mesh with a given velocity in a virtual endless computation area. As a result the inflow flux correlates to the given relative velocity which in the end produces surface loads, similar to the commonly used inflow condition Ma $\neq$ 0.

3.2. Mesh Convergence Study

The Mesh Grid Convergence Index (GCI) of the used inviscid mesh is presented in an earlier work [4]. The mesh showed a good trade-off between accuracy and computational cost with an GCI $<$ 4.7 % at 4.6 M Points. At low speed the GCI $<$ 3.8 %, where in supersonic regimes it is well under 1 %, shown in figure 3.

For the unsteady viscous calculations a mesh with a decent boundary layer approximated by prismatic cells had to be generated, which is rather difficult for the given trajectory case. As the velocity rises over flight time, the boundary layer gets smaller. Which leads to unnecessary fine cells on the outside of the boundary layer, as the maximum height had to match the critical low speed case. On the other end of the trajectory at high supersonic speed the boundary layer defines the smallest first cell height to get an $y^+ < 1$ over the whole trajectory, which makes the mesh unnecessarily fine resolved at low the subsonic regime.

A good compromise was found with a smallest layer height of 1×10^{-6} m and 27 layers with a constant growing factor of around 1.4 leading to a maximal thickness of 0.0216 m. This mesh produces an GCI $<$ 3.2 % as shown in figure 3 for a constant refinement factor R $=$ 1.3 at a critical low subsonic Ma $=$ 0.4. On this basis the normal mesh with 27 boundary layer prismatic cells is used for the viscous calculations.

The surface mesh of the viscous URANS simulations was obtained from the best performing non-viscous mesh.

3.3. Empirical Mode Decomposition of Wind Profiles

Weather balloons and their attached radio sondes are exposed to multiple unsteady phenomena which might cause the balloon as well as the data acquiring radio sonde to show arbitrary (self-induced) motions, e. g. sudden changes in the wind vector [14] or a fluctuating wake of the balloon due to a turbulent boundary layer [7] depending on the Reynolds number with similar effects as the van Kármán vortex street. These motions can be noticed in the recorded wind data and need to be filtered before

Copyright © 2022 by the author(s)

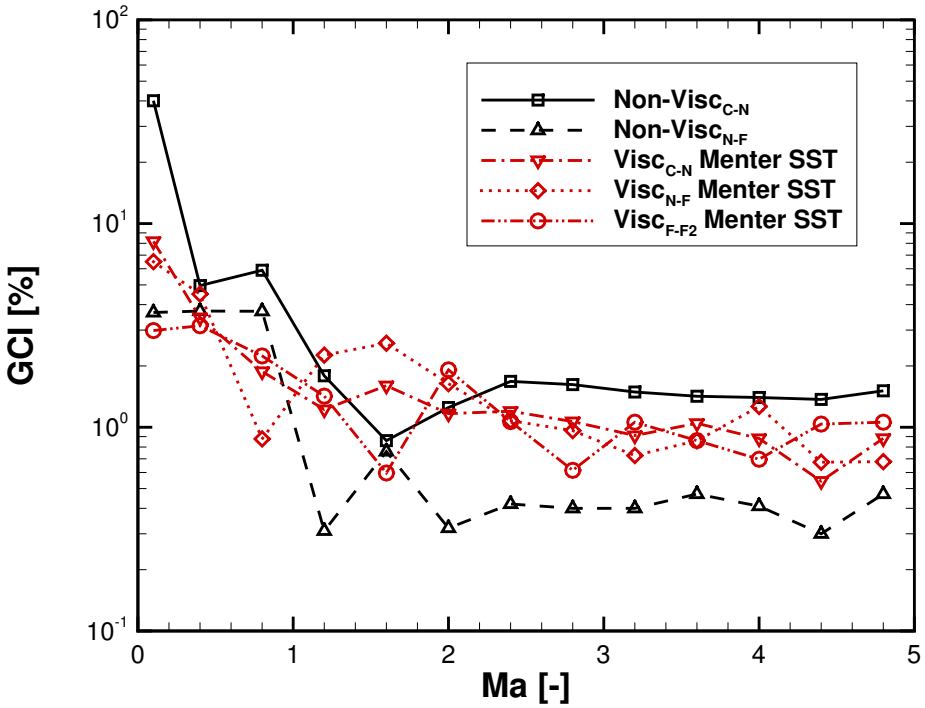

Fig 3. Grid Convergence Index of body force coefficients for inviscid and boundary layer variation of viscid simulations for the coarse (C), normal (N) and fine (F) mesh.

using the wind profiles in the further process. This paper uses the Empirical Mode Decomposition as presented in Sako [7] to do the filtering. Figure 4 shows the power spectral densities for the wind profiles of all seven weather balloons. It is easy to see that AND1 and AND2 show a, for self-induced balloon motions, characteristic large peak at 0.1 Hz. Hence, the wind profiles of Bjørnøya and Jan Mayen were probably pre-filtered by other methods or in the case of the Spitsbergen balloon the sampling rate of 0.2 Hz is too large to capture those frequencies.

Nevertheless, the wind profiles of Bjørnøya, Jan Mayen and Spitsbergen still show rather frequent fluctuations which are not expected to have any influence on the results due to the large speed of SHEFEX II compared to the wind speeds. Thus, all wind profiles are filtered, i. e. not only the arbitrary (self-induced) motions are filtered, but also remaining frequent wind fluctuations to obtain a smooth trend for the wind profiles. The actual filtering is done visually by calculating IMF decompositions for different abort criteria in the region of $10^{-6} \leq \epsilon_{\text{STOP}} \leq 10^{-3}$ and finding a suitable combination of subtracted IMFs which represent the trend of the wind profiles best. As can be seen in figure 5, subtracting the IMFs from the raw signal reduces the fluctuation and smooths the curve, i. e. filters the balloon induces oscillation as well as small gusts, leaving the main wind profile. The abort criteria for the IMF sifting are shown in table 2.

Table 2. Abort criteria ϵ_{EMD} and number of substracted IMF of weather ballons AND1, BJO2, JAN2 and SPI.

	AND1		**BJO2**		**JAN2**		**SPI**	
wind component	U_w	V_w	U_w	V_w	U_w	V_w	U_w	V_w
ϵ_{EMD}	10^{-5}		10^{-3}		10^{-4}		10^{-6}	
IMF	7	7	5	4	5	4	4	4

Copyright © 2022 by the author(s)

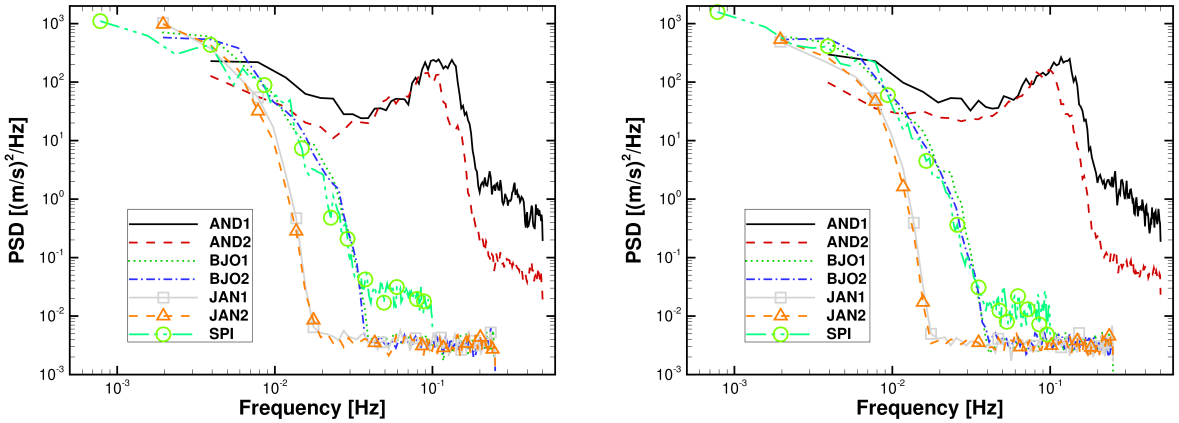

(a) North direction (U). (b) East direction (V).

Fig 4. Power spectral densities of the wind profiles of the seven weather balloons.

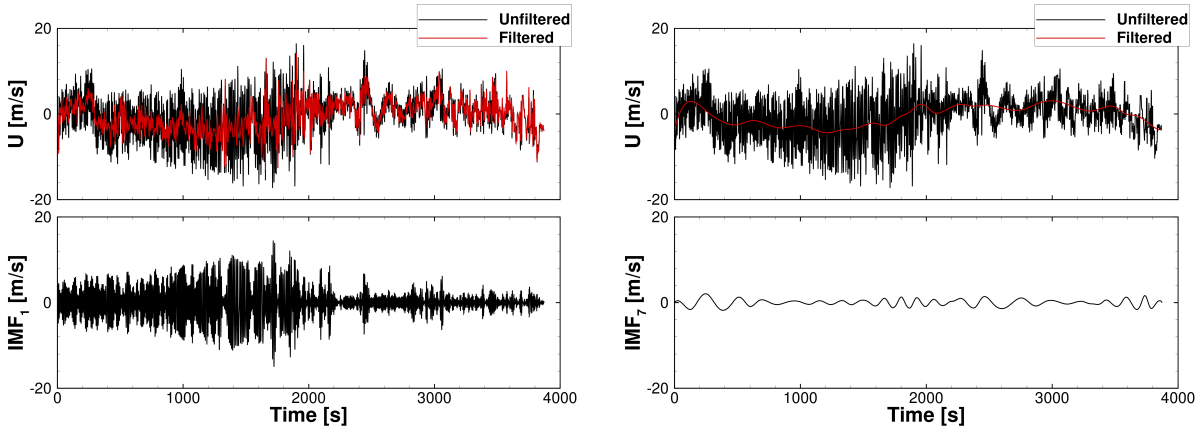

(a) Unfiltered data with subtracted IMF 1. (b) Unfiltered data with subtracted IMFs 1 to 7.

Fig 5. Filtered wind profile of AND1 using different IMFs.

Copyright © 2022 by the author(s)

3.4. Interpolation using Radial Basis Functions

The processed weather balloon data is combined into an atmospheric model using radial basis function interpolation of the atmospheric parameters as well as SHEFEX II's GPS position and altitude data. The interpolation process bases on the implementation of the RBF interpolation method in the well known Python module "SciPy" with its function "scipy.interpolate.Rbf()". Each atmospheric parameter is interpolated at specific altitude layers and afterwards evaluated at the current position of SHEFEX II in this altitude in order to get a three dimensional weather model for the launch phase of SHEFEX II.

To identify a suitable RBF, a parameter study with all RBFs available in "scipy.interpolate.RbF()" is carried out based on the outer pressure near the ground. The idea behind choosing this setup is that it is much simpler to identify unrealistic pressure values and, therefore an unrealistic interpolation, than unrealistic temperature or wind values as well as unrealistic values in the upper atmosphere.

During the parameter study the interpolation process proved to be very sensitive concerning the form parameter ϵ of the infinitely smooth RBFs when all balloons from Andøya, Bjørnøya and Jan Mayen are utilised as sampling points for the interpolation. Therefore, only one balloon per station (AND1, BJO2 and JAN2) is used, as this combination shows a much less sensitive behaviour. The multiquadric RBF proves to be suitable with a form parameter of $\epsilon = 10^8$.

This reduced supporting point approach has, however, disadvantages at an altitude of h ≈ 27.2 km where no data of the AND1 balloon is available anymore. The still large distance between the position of SHEFEX II at this altitude and the Spitsbergen balloon acts as a kind of "lever" so that the wind velocities of the Spitsbergen balloon are nearly projected one-on-one with inverted sign into the atmospheric model. Since the wind velocities at Spitsbergen are large compared to BJO2 and JAN2 neglecting the Spitsbergen balloon completely seems to be a more conservative approach for the atmosphere above h ≈ 27.2 km. The resulting discontinuity at h ≈ 27.2 km which arises due to the fact that AND1 is no longer available as sampling point, is smoothed by applying a linear weighting function in the region of 24.5 km $\leq$ h ≤ 27.183 km.

4. Results of Analysis

4.1. New Atmospheric Model

Figure 6(a) illustrates the new atmospheric model (IATM - interpolated atmosphere model) by means of outer temperature and pressure. For the sake of comprehension the atmospheric model presented by Franze [3] (LATM - linear averaged atmosphere model) is depicted as well. In the following, IATM denotes the interpolated atmospheric model without wind model and IATM$^{(W)}$ the interpolated model including wind. One can clearly see that the outer pressure curves show hardly any differences ($\Delta p_{max} = 6.27$ hPa at h $= 469$ m) between IATM and LATM whereas the curves of outer temperature differ to a larger extend. The maximum difference occurs right at the beginning of the flight with $\Delta T_{max} = 3.95$ K. As both differences are small compared to the absolute values of the atmospheric parameters, no big differences in the fin loadings are expected between the two cases LATM and IATM. It is noted that calculating the tropopause in accordance to the definition of the U.S. Department of Commerce/National Oceanic and Atmospheric Administration [10] a difference of about 600 m between the two atmospheric models with $h_{tropo,\ LATM} = 9959$ m and $h_{tropo,\ IATM} = 9376$ m can be seen.

Figure 6(b) shows the created wind model for the flight of SHEFEX II with its wind components U (acting in north-south direction) and V (acting in east-west direction) and their resulting value, presenting values fluctuating between 0 m/s to 9 m/s, depending on the altitude.

4.2. Angle of Attack Oscillations

Figure 7 plots the total angle of attack calculated from the HNS data over the first 55 s of the flight trajectory against the total angle of attack if the wind profile shown in figure 6(b) is added.

The first 10 s show the transient effect from the initial pitching from the starting ramp. Afterwards the total angle of attack does not exceed $\alpha < 1.5°$ from 10 s to 55 s. The wind profile adds a significant amount to the resulting total angle of attack, oscillating between $-1° < \alpha_w < 1°$ by itself, leading to twice the amount of the value at the beginning. This indicates a huge effect of the wind for the

Copyright © 2022 by the author(s)

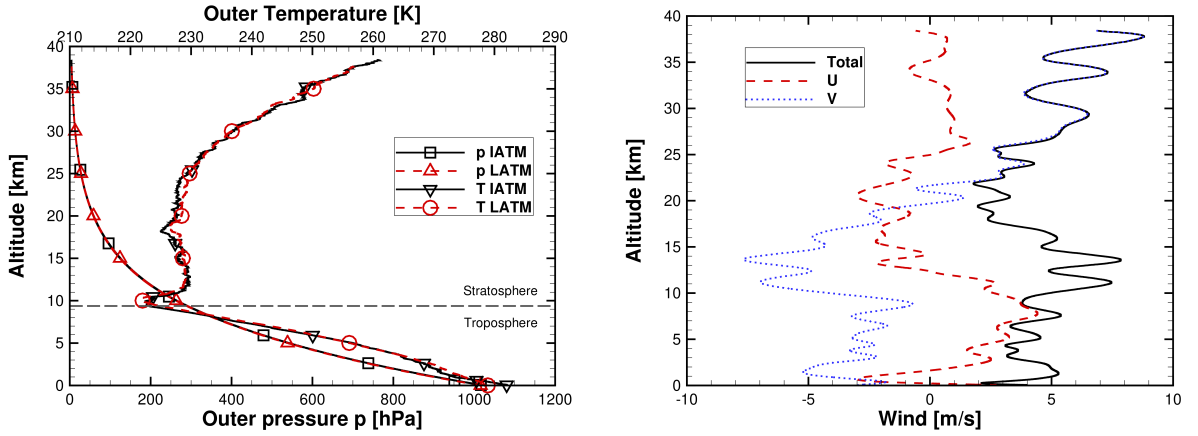

(a) Atmospheric models. (b) Wind component U: north → south - V: east → west.

Fig 6. Used atmospheric and wind models.

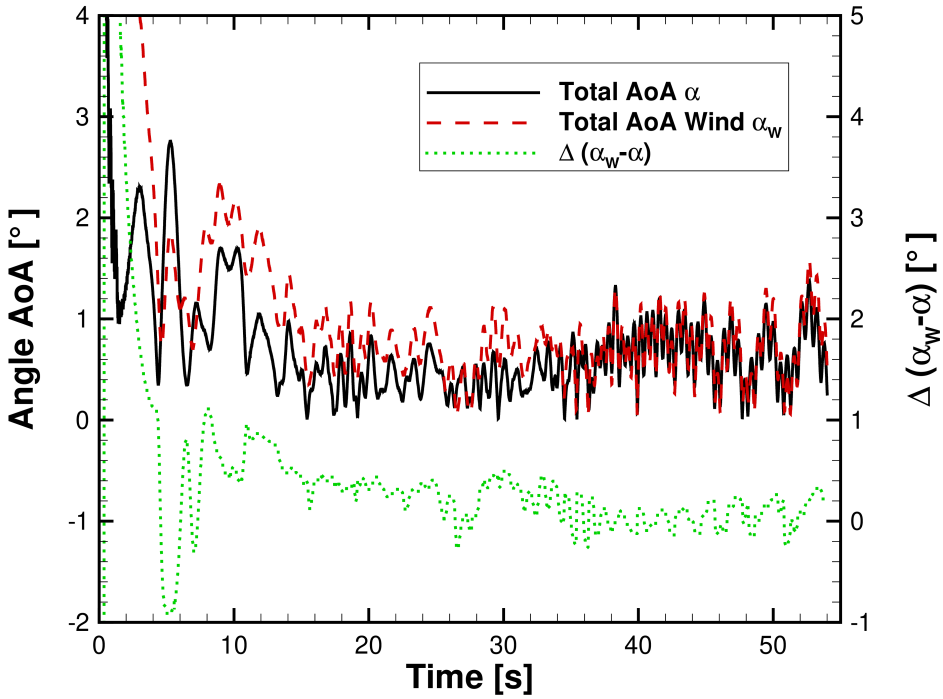

Fig 7. Angle of Attack vs. Flight time and corresponding wind influence.

Copyright © 2022 by the author(s)

aerodynamic loading on the vehicle, which is mainly depending on the velocity and the total angle of attack. As the time proceeds, the velocity of the sounding rocket rises, which reduces the impact of the wind, as it does not exceed 9 m/s.

4.3. Maximum Loads During the Ascend Phase using inviscid calculations

4.3.1. Drag Force and Roll Moment

The total Drag force, as can be seen in figure 8 has an asymptotic trend at both end of the computed time range. At the start the velocity is small and the outer density is high, which leads to the increasing force and roll moment. Between $10\,s < t < 15\,s$ small oscillations indicate the transsonic phase of the ascend. Afterwards the dynamic pressure rises and the maxima for both roll axes force as well as roll moment peaks at around 20 s and 25 s respectively. Due to the decreasing density and therefore dynamic pressure the curves approximate to zero. Additionally in the end the roll rate reaches its maximum resulting in a decreasing roll moment over time, as the effective angle of attack of the fixed fins decreases. Furthermore the atmosphere model has only minor influences on the results.

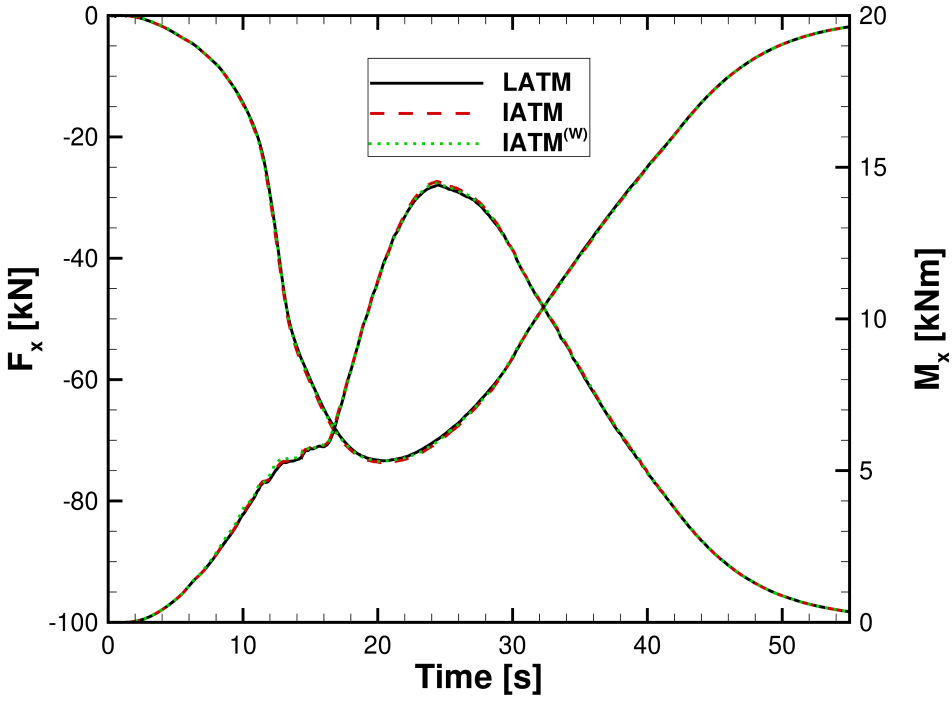

Fig 8. Drag force and Roll moment at different atmosphere models.

4.3.2. Fin Forces

Figure 9 shows the oscillation of the perpenticular forces of Fin 9 (the four fins are named according to the clock-face in counter-clockwise direction when looking from the back of SHEFEX II) exemplarily for all four fins. The oscillations start at zero and their frequency increases as the roll rate increases over flight time. Due to the roll stabilized precession shown in figure 7 each fin rotates upwind and downwind resulting in the shown oscillations. As the dynamic pressure has its maximum between $10\,s < t < 15\,s$ the biggest absolute force differences are in this time slot. As the final roll rate is developing and the dynamic pressure reduces the oscillating fin loading approximates to zero. To compare different atmospheric influences in the following the force magnitude is calculated and presented with F_{yz}.

Figure 10(a) and 10(b) show exemplarily the calculated force magnitude at Fin 6 and Fin 9 of the first stage of SHEFEX II for all three atmospheric models. As already stated above, LATM and IATM show hardly any differences in the forces. Introducing the wind model with IATM$^{(W)}$ has, as predicted, a large influence on the calculated forces.

Copyright © 2022 by the author(s)

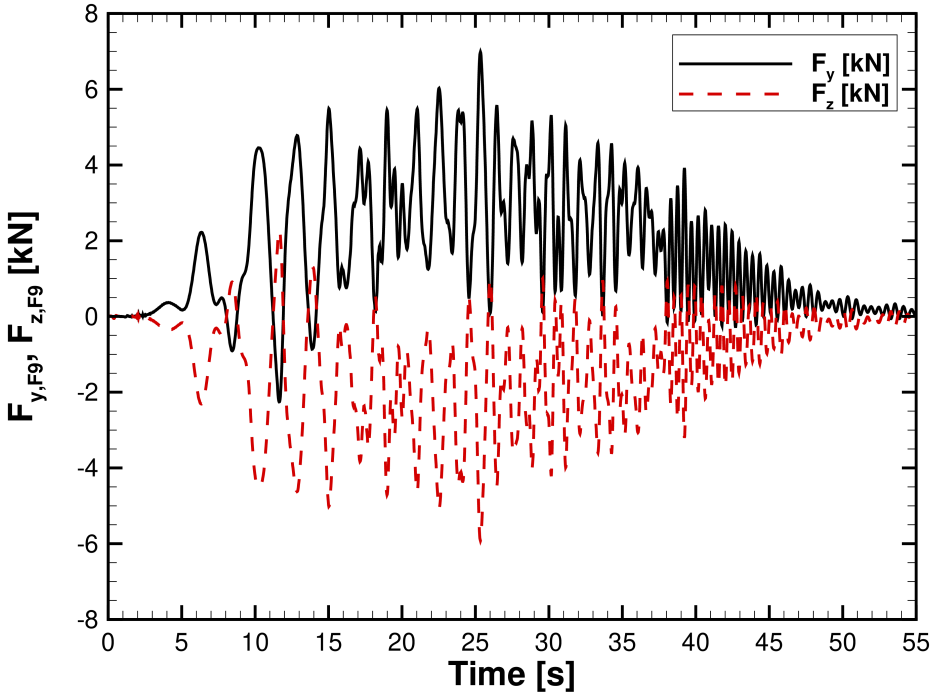

Fig 9. Perpenticular Aerodynamic Forces on Fin 9.

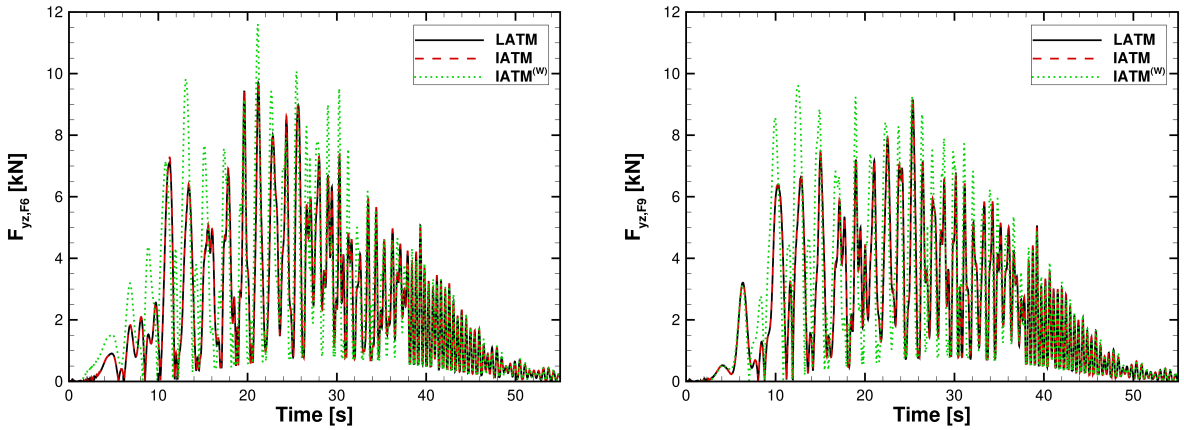

(a) Force Magnitude acting perpendicular to Fin 6.

(b) Force Magnitude acting perpendicular to Fin 9.

Fig 10. Fin loading over flight time of two perpenticular oriented fins.

Copyright © 2022 by the author(s)

The force component perpendicular to the fin changes its intensity on a regular basis. This is due to the induced roll motion of SHEFEX II. One can clearly notice that the maximum force fluctuations increase dramatically when wind is added to the simulations. On Fin 6 for LATM and IATM, the maximum fluctuation are $F_{yz,F6,max} = 9.6$ kN at 21.17 s compared to $F_{yz,F6,max} = 11.5$ kN ($+20$ %) for IATM$^{(W)}$. Both values are at the same flight time point in the supersonic flight path regime.

On the other hand at Fin 9 the maximum fluctuations are $F_{yz,F9,max} = 9.2$ kN at 25.36 s for LATM and IATM compared to $F_{yz,F9,max} = 9.6$ kN at 12.55 s ($+4$ % at different flight time). This means that the maximum force fluctuation occurs within the transonic region for IATM$^{(W)}$ and in the supersonic region for the other two models. The transonic region spans roughly from 11.5 s to 19.5 s flight time with Mach numbers between $0.9 \leq$ Ma ≤ 1.5. One can further observe that the force fluctuation in the transonic region almost double for IATM$^{(W)}$. Nevertheless, as the force fluctuation increase in both directions almost equally no major differences in the acting roll moment can be observed throughout the launch phase between all three atmospheric models.

Overall, figure 10 shows that the relative increase of the maximum force component has its largest increases in the transonic region with relative increases up to ca. 85 % in the transsonic region leading to a time shift of the critical point regarding fin loading as the maximum dynamic pressure occurs at higher mach numbers as well as flight time.

After 37 s flight time, the differences between the results of all atmospheric models are negligible and as SHEFEX II is still well below the maximum altitude of AND1 the utilised conservative approach of neglecting the Spitsbergen balloon completely shows no negative influence on the results.

4.4. Maximum Loads During the Ascend Phase using uRANS

As discussed in the former section, the biggest influence of the wind model is in the sub- and transonic region of SHEFEX II up until ca. 22 s, where viscous effects can have a significant influence. For this reason, a viscous URANS (unsteady RANS) calculation using a central scheme is performed on basis of the LATM model, i. e. without the influence of wind.

Figure 11 shows that overall the viscous effects are hard to see and negligible compared to the wind effects. Reasons can be found in the rather simple geometry of SHEFEX II with clear sharp edges, where it is easy for the turbulence model to predict flow separation. These specific pressure grandients are calculated by the inviscid Euler simulations as well. Only minor differences are noticeable in the peak loading at 11.25 s (9 %) for Fin 6 and at 10.26 s (-4 %) for Fin 9, but for the most part of the trajectory the results match between the two different calculations.

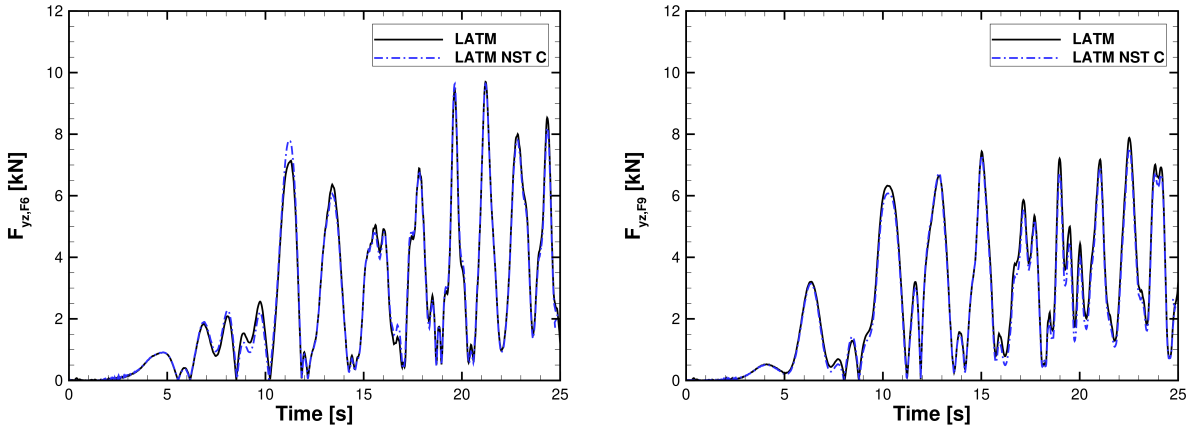

(a) Force Magnitude acting perpendicular to Fin 6.

(b) Force Magnitude acting perpendicular to Fin 9.

Fig 11. Fin loading over flight time of two perpenticular oriented fins, inviscid vs. viscous calculations.

For further investigations of the SHEFEX II trajectory it is suitable to calculate inviscid Euler simulations.

Copyright © 2022 by the author(s)

Especially due to the computational cost savings.

5. Conclusions and Outlook

Firstly, this work post processes the collected wind data from the start of SHEFEX II and filters it by means of their intrinsic mode functions using an empirical mode decomposition to extract the wind profiles of the starting conditions and reduce measurement errors due to wind balloon oscillations.

Secondly, the generated atmosphere and wind profile is compared to a simpler linear interpolation method from an earlier work. The differences are small comparing the different atmospheric parameters temperature, density and pressure, but significant if the wind is considered in the simulations. At certain points the wind induces twice the amount of dynamical loading on the fins of SHEFEX II potentially leading to different free flight values.

As the most differences are seen in the sub- and transonic regions, viscous URANS simulation are performed additionally to eliminate the uncertainty of surface friction in the results, but simulations show that the viscous effect can be neglected mainly due to the simple geometry.

Next, a fully coupled fluid structure trajectory simulation (CFD-CSM-CFM) is implemented to evaluate the influence of the fin loading and their resulting fin deformation on the flight trajectory of SHEFEX II.

References

[1] Javier Bartolome Calvo and Thino Eggers. Application of a Coupling of Aerodynamics and Flight Dynamics to the SHEFEX I Flight Experiment. *17th AIAA International Space Planes and Hypersonic Systems and Technologies Conference, AIAA Paper 2011-2323*, pages 1–12, 2011.

[2] Thino Eggers, Andreas Stamminger, Marcus Hörschgen, Wolfgang Jung, and John Turner. The Hypersonic Experiment SHEFEX - Aerothermodynamic Layout, Vehicle Development and First Flight Results. *Proceedings of 6th International Symposium on Launcher Technologies 'Flight Environment Control for Future and Operational Launchers'*, 2005.

[3] Marius Franze. SHEFEX II - A First Aerodynamic and Atmospheric Post-Flight Analysis. In *AIAA Atmospheric Flight Mechanics Conference*, San Diego, 2016.

[4] Marius Franze. SHEFEX II - An Aerodynamic and Structural Post-Flight Analysis. In *AIAA Atmospheric Flight Mechanics Conference*, Washington D.C., 2016.

[5] Ralf Heinrich and Andreas Michler. Unsteady Simulation of the Encounter of a Transport Aircraft with a Generic Gust by CFD Flight Mechanics Coupling. In *Proceedings of the CEAS Conference*, Manchester, United Kingdom, 2009.

[6] A. Mack and Volker Hannemann. Validation of the Unstructured DLR-TAU-Code for Hypersonic Flows. In *32nd AIAA Fluid Dynamics Conference and Exhibit, AIAA Paper 2002-3111*, pages 1–9, St. Lousi, Missouri, 2002.

[7] Brian H. Sako. Empirical Mode Decomposition Filtering of Wind Profiles. *AIAA Atmospheric Flight Mechanics Conference*, (January):1–23, 2016.

[8] Dieter Schwamborn, Thomas Gerhold, and Ralf Heinrich. The DLR TAU-Code: Recent Applications in Research and Industry. *European Conference on Computational Fluid Dynamics, ECCOMAS CFD*, pages 1–25, 2006.

[9] Stephen Steffes. Real-Time Navigation Algorithm for the SHEFEX2 Hybrid Navigation System Experiment. In *AIAA Guidance, Navigation and Control Conference, AIAA Paper 2012-4990*, pages 1–19, 2012.

[10] U.S. Department of Commerce / National Oceanic and Atmospheric Administration. Federal Meteorological Handbook No. 3 - Rawinsonde and Pibal Observations. 1997.

[11] Yasuhiro Wada and Meng-Sing Liou. A flux splitting scheme with high-resolution and robustness for discontinuities. *AIAA paper 94-0083*, pages 1–23, 1994.

Copyright © 2022 by the author(s)

[12] Hendrik Weihs. Sounding Rockets for Entry Research : SHEFEX Flight Test Program. *Proceedings of the 21st ESA Symposium on Rocket and Balloon Programmes*, SP-721:143–152, 2013.

[13] Hendrik Weihs, José M. A. Longo, and John Turner. The Sharp Edge Flight Experiment SHEFEX II, a Mission Overview and Status. *15th AIAA International Space Planes and Hypersonic Systems and Technologies Conference, AIAA Paper 2008-2542*, pages 1–14, 2008.

[14] Nobuyuki Yajima, Naoki Izutsu, Takeshi Imamura, and Toyoo Abe. *Scientific Ballooning: Technology and Applications of Exploration Balloons Floating in the Stratosphere and the Atmospheres of Other Planets*. Springer-Verlag New York, first edition, 2009.

Copyright © 2022 by the author(s)